Mass Models of the Milky Way and Estimation of Its Mass from the Gaia DR3 Data Set

Francesco Sylos Labini[1,2] , Žofia Chrobáková[3] , Roberto Capuzzo-Dolcetta[1,4], and Martín López-Corredoira[5,6]

[1] Centro Ricerche Enrico Fermi, Via Panisperna 89a, I-00184 Rome, Italy; sylos@cref.it
[2] Istituto Nazionale Fisica Nucleare, Unità Roma 1, Dipartimento di Fisica, Universitá di Roma "Sapienza," I-00185 Rome, Italy
[3] Faculty of Mathematics, Physics, and Informatics, Comenius University, Mlynská dolina, 842 48 Bratislava, Slovakia
[4] Dipartimento di Fisica, Universitá di Roma "Sapienza," I-00185 Rome, Italy
[5] Instituto de Astrofísica de Canarias, E-38205 La Laguna, Tenerife, Spain
[6] Departamento de Astrofísica, Universidad de La Laguna, E-38206 La Laguna, Tenerife, Spain

Abstract

We use data from the Gaia DR3 data set to estimate the mass of the Milky Way (MW) by analyzing the rotation curve in the range of distances 5 to 28 kpc. We consider three mass models: The first model adds a spherical dark matter (DM) halo, following the Navarro–Frenk–White (NFW) profile, to the known stellar components. The second model assumes that DM is confined to the Galactic disk, following the idea that the observed density of gas in the Galaxy is related to the presence of a more massive DM disk (DMD), similar to the observed correlation between DM and gas in other galaxies. The third model only uses the known stellar-mass components and is based on the Modified Newton Dynamics (MOND) theory. Our results indicate that the DMD model is comparable in accuracy to the NFW and MOND models and fits the data better at large radii where the rotation curve declines but has the largest errors. For the NFW model, we obtain a virial mass $M_{\rm vir} = (6.5 \pm 0.3) \times 10^{11} M_{\odot}$ with concentration parameter $c = 14.5$, which is lower than what is typically reported. In the DMD case, we find that the MW mass is $M_d = (1.6 \pm 0.5) \times 10^{11} M_{\odot}$ with a disk's characteristic radius of $R_d = 17$ kpc.

Unified Astronomy Thesaurus concepts: Milky Way Galaxy (1054)

1. Introduction

Determining the Milky Way's (MW's) mass profile requires measuring its midplane circular velocity $v_c(R)$. The rotation curve has been measured using different methods and kinematical data on a variety of tracer objects (see, e.g., Bhattacharjee et al. 2014; Sofue 2020 and references therein). However, in most cases, the full three-dimensional velocity information of the tracers is not available, so the circular velocity had to be estimated using only the measured line-of-sight velocity and position. Uncertainties in distance estimates, limited numbers of tracers, and their uneven distribution can introduce significant errors in the analysis of the circular velocity curve.

To accurately determine the MW's rotation curve $v_c(R)$, we need precise measurements of the Galactocentric radius R, tangential velocity, and radial velocity for each star, including the position and velocity uncertainties in all three spatial dimensions. The Gaia mission (Gaia Collaboration et al. 2016), by measuring the astrometry, photometry, and spectroscopy of a large number of stars, is providing the position and velocity information in all six dimensions for a large sample of stars in the MW. These data are thus ideal to measure the Galaxy rotation curve $v_c(R)$.

Recently, three independent research groups (Eilers et al. 2019; Mróz et al. 2019; Wang et al. 2023) have used the Gaia data sets to determine the MW rotation curve, with measurements based on different samples of stars. The first two measurements are based on red giant stars and Cepheids, respectively, while the third uses a statistical deconvolution

method applied to the entire data set. These measurements show a similar slow declining trend in different but overlapping distance ranges between 5 and 28 kpc.

It is clear that the mass estimated when the rotation curve declines is lower than that measured when $v_c(R) \approx$ const. Indeed, Eilers et al. (2019), by considering the standard Navarro, Frenk, and White (NFW) halo model (Navarro et al. 1997), found a virial mass of $M_{\rm vir} = (7.25 \pm 0.25) \times 10^{11} M_{\odot}$ (with $R_{\rm vir} = (189.3 \pm 2.2)$ kpc), which is significantly lower than what several previous studies suggest (see, e.g., Watkins et al. 2019), although values reported in the literature span approximately in the range $(0.5–3) \times 10^{12} M_{\odot}$ (see, e.g., Bland-Hawthorn & Gerhard 2016 and references therein).

In this paper we combine the determination of the rotation curve derived by Eilers et al. (2019), in the range of Galactocentric radii 5–25 kpc, with that by Wang et al. (2023), in the range 8–28 kpc, to make an estimation of the mass of the MW under three different theoretical mass models. The first theoretical mass model we are using is the canonical NFW halo model (Navarro et al. 1997), which assumes that the visible matter of the MW is confined to a rotationally supported disk embedded in a much heavier halo of dark matter (DM). As the study by Wang et al. (2023) found that the declining trend in the rotation curve continues at greater distances, we expect that this mass model would predict a lower value of the MW's mass than the one estimated by Eilers et al. (2019).

The second theoretical mass model assumes that DM is confined to a relatively thin disk, similar to the visible disk. The motivation for this model comes from the "Bosma effect" (Bosma 1978, 1981), which suggests a correlation between DM and gas in disk galaxies. Indeed, there is substantial observational evidence that rotation curves of disk galaxies are, at large enough radii, a rescaled version of those derived from the distribution of gas (Sancisi 1999; Hoekstra et al. 2001). It is important to note that the correlation between gas

and DM observed in disk galaxies does not necessarily imply causality. It is worth exploring the possibility that by assuming that the distribution of gas is a tracer of the distribution of DM, we can find a different mass model than the standard NFW one that fits the observed rotation curve of the MW with similar accuracy, as it has been observed in a number of external galaxies by Hessman & Ziebart (2011) and Swaters et al. (2012). In the DM disk (DMD) model, where DM is assumed to be confined to a relatively thin disk similar to the visible disk, the total mass of the Galaxy is expected to be lower than in the case of a spherical halo, as the mass is concentrated in a thinner region.

The third theoretical mass model is based on the framework of Modified Newtonian Dynamics (MOND) (Milgrom 1983; Scarpa 2006; McGaugh et al. 2016). This model does not require the introduction of an additional DM component and only considers the mass of the visible stellar components. In this model, the gravitational force is assumed to decline more slowly than in Newtonian dynamics, which allows for the rotation curve to remain steady without the need for additional mass beyond the visible stellar components.

The paper is organized as follows. In Section 2, we discuss the main characteristics of the "Bosma effect" and its observational evidence. In Section 3, we briefly review the measurements of the rotation curve based on the Gaia data sets that we use in this work. In Section 4, we discuss the different mass models and present their fits to the rotation curve. Finally, in Section 5, we discuss the results obtained, draw our main conclusions, and mention the possible dynamical implications.

2. The Bosma Effect

Bosma (1978, 1981) first noticed a correlation between the centripetal contribution of the atomic hydrogen H I gas, which is dynamically insignificant, in the disks of spiral galaxies and the dominant contribution of DM. This correlation is known as the "Bosma effect" and has been observed by multiple studies (Sancisi 1999; Hoekstra et al. 2001). The effect is thought to reveal a relationship between the visible baryonic matter and the invisible DM. For example, Hoekstra et al. (2001) examined a sample of disk galaxies with high-quality rotation curves and found that, with a few exceptions, the rotation curves generated by scaling up the centripetal contribution of the H I gas by a constant factor of about 10 and not including a spherical DM halo were similar in accuracy to those generated by the NFW halo model.

It should be noted that Hoekstra et al. (2001) defined the constant of proportionality between the centripetal effects of the H I gas and the DM as the assumed constant ratio of the DM to H I surface densities, averaged over the disk. This ratio was corrected only for the presence of helium, which is a small fraction of the total gas mass. Bosma's original concept was to use the total gas surface density as a proxy for DM, including not only H I but also other components of the interstellar medium (ISM). Hessman & Ziebart (2011) distinguished between the "simple" Bosma effect, which is the case where only the surface density of H I (corrected for the contribution of He and heavy elements) is used as a proxy for the distribution of DM, and the "classic" Bosma effect, which includes the total gaseous surface density not only of H I but of other components of the ISM. This can be done explicitly by using the surface density of the ISM defined as $\Sigma_{\mathrm{ISM}} = \Sigma_{\mathrm{HI}} + \Sigma_{\mathrm{H_2}}$

(again corrected for He and heavy elements), or implicitly by using the stellar disk as an additional proxy.

The reason for this inclusion is that, from a physical point of view, it is expected that the correlation between DM and the ISM would be with the total ISM, not just its neutral hydrogen (H I) component. This is because the total ISM, including both neutral and ionized gas, is thought to be more closely related to the distribution of DM than just the neutral H I component alone.

Hessman & Ziebart (2011) used the stellar disk as an additional proxy of the DM component because the H I surface density does not reflect the total gas surface density in the inner galactic region. They confirmed the correlation between DM and H I distribution using several galaxies from The H I Nearby Galaxy Survey data set (De Blok et al. 2008) and rebutted several arguments against the effect by Hoekstra et al. (2001). They found fits of similar or even better quality than those obtained by the standard NFW halo model.

Swaters et al. (2012) further studied a sample of 43 disk galaxies by fitting the rotation curves with mass models based on scaling up the stellar and H I disks. They found that such scaling models fit the observed rotation curves well in the vast majority of cases, even though the models have only two or three free parameters (depending on whether the galaxy has a bulge or not). They also found that these models reproduce some of the detailed small-scale features of rotation curves such as the "bumps" and "wiggles."

In summary, the "Bosma effect" implies a close connection between the ISM and the DM and points toward a baryonic nature and a more or less flat distribution of the dark component. This could be in the form of very dense cold gas distributed in molecular clouds in galactic disks, as suggested by studies such as Pfenniger et al. (1994) and Revaz et al. (2009).

3. Rotation Curve of the Milky Way

3.1. The Data

Three independent determinations of the MW rotation curve have been obtained from different samples based on the Gaia data, which reasonably agree with each other. These samples cover the range of distances between 5 kpc and 28 kpc, but each of them only partially. In the overlapping range of radii, they show reasonable agreement. The common feature is that the rotation curve, $v_c(R)$, presents a declining behavior with the cylindrical radius, R.

The first analysis was provided by Mróz et al. (2019), who built and analyzed a sample of 773 Classical Cepheids with precise distances based on mid-infrared period–luminosity relations, coupled with proper motions and radial velocities from Gaia, in the range of radii between 5 and 20 kpc. However, the number of Cepheids significantly decreases for $R > 15$ kpc, which limits the well-sampled range of distances to 15 kpc. They found that

$$v_c(R) = v(R_\odot) + \beta(R - R_\odot), \qquad (1)$$

where $R_\odot = 8.122 \pm 0.031$ kpc (GRAVITY Collaboration et al. 2018) is the distance of the Sun from the Galactic center, $v(R_\odot)$ is the rotation speed of the Sun, and the slope was determined to be $\beta = -(1.4 \pm 0.1)$ km s^{-1} kpc^{-1}.

The second measurement was made by Eilers et al. (2019) by using the spectral data from APOGEE DR14, the photometric

information from Gaia Data Release 2 (DR2), 2MASS, and the Wide-field Infrared Survey Explorer. They built a sample of 23,000 red giant stars with the whole 6D spatial and velocity information. The sample is thus characterized by precise and accurate distances to luminous tracers that can be observed over a wide range of Galactic distances. They derived the rotation curve for Galactocentric distances between 5 kpc and 25 kpc and found a slope $\beta = -(1.7 \pm 0.1)$ km s^{-1} kpc^{-1} that is in reasonably good agreement with that of Mróz et al. (2019) considering the former covers the range $\approx$5–15 kpc while the latter 5–25 kpc.

The third determination was made by Wang et al. (2023) who have adopted the statistical inversion method introduced by Lucy (1977) to reduce the errors in the distance determination in the Gaia DR3 data set beyond 20 kpc. That method was first applied by López-Corredoira & Sylos Labini (2019) to the Gaia DR2 sources to measure their three-dimensional velocity components in the range of Galacto-centric distances between 8 and 20 kpc with their corresp-onding errors and rms values. Wang et al. (2023) have extended the analysis to $\approx$28 kpc by considering the Gaia DR3 sources (Gaia Collaboration et al. 2022), and they have obtained results for the three velocity components in agreement with those measured by López-Corredoira & Sylos Labini (2019). In addition, the rotation curve $v_c(R)$ obtained by Wang et al. (2023) is in reasonable agreement with the measurements by Mróz et al. (2019) and Eilers et al. (2019). In particular, the slope of Equation (1) was $\beta = -(2.3 \pm 0.2)$ km s^{-1} kpc^{-1}, i.e., a faster declining slope than the other two determinations mentioned above. However, in the range of radii where they overlap, the three measurements are in reasonably good agreement with each other.

We use the determinations by Wang et al. (2023) with that of Eilers et al. (2019) to construct the rotation curve in the range 5–28 kpc. We report in Table 1 the values of the rotation curve in bins of size $\Delta R = 0.5$ kpc, and we label this rotation curve DR3+ to distinguish from the determinations of Eilers et al. (2019) (E19) and of Wang et al. (2023) (DR3). In what follows we will provide fits with different mass models for all three measurements of the rotation curve.

3.2. Discussion

The Galaxy rotation curve is obtained by using the time-independent Jeans equation in an axisymmetric gravitational potential and assuming a smooth and monotonic density distribution (see Equations (7)–(10) of Wang et al. 2023). This basic assumption is used to link the moments of the velocity distribution and the density of a collective of stars to the gravitational potential and to derive the Jeans equation (Binney & Tremaine 2008). However, simplifications are often made, such as ignoring terms with v_Z in the Jeans equation (Eilers et al. 2019; Wang et al. 2023) and nonmonotonic variations in the surface density profile, such as localized structures like spiral arms, as these may cause deviation from the smooth models that are generally assumed (McGaugh 2016). These structures show that the assumption of a time-independent gravitational potential is only a rough approximation to the actual dynamics.

The observed velocity field in the galaxy has been found to have asymmetrical motions with significant gradients in all velocity components (Antoja et al. 2018; Gaia Collaboration et al. 2018; López-Corredoira & Sylos Labini 2019;

Table 1
Measurements of the Circular Velocity of the Milky Way for the DR3+ Rotation Curve (See Text)

R (kpc)	v_c (km s^{-1})	σ_{v_c} (km s^{-1})
5.25	226.8	1.9
5.75	230.8	1.4
6.25	231.2	1.4
6.75	229.9	1.4
7.25	229.6	1.2
7.75	229.9	0.9
8.25	228.9	0.7
8.75	224.2	2.4
9.25	223.8	2.0
9.75	223.7	2.2
10.25	224.5	1.8
10.75	223.6	1.8
11.25	222.2	2.0
11.75	222.4	1.8
12.25	222.0	1.9
12.75	222.4	2.2
13.25	223.1	1.8
13.75	220.5	1.9
14.25	219.5	2.3
14.75	219.3	1.9
15.25	218.0	2.1
15.75	217.6	2.4
16.25	216.4	2.4
16.75	214.0	2.4
17.25	215.1	2.8
17.75	213.3	2.7
18.25	208.9	2.7
18.75	209.1	3.4
19.25	206.9	3.2
19.75	203.4	3.3
20.25	201.2	3.5
20.75	200.1	3.5
21.25	197.3	5.3
21.75	205.2	9.2
22.25	184.0	13.5
22.75	194.4	13.4
23.25	195.2	4.5
23.75	185.1	9.7
24.25	196.3	1.7
24.75	193.4	3.7
25.25	190.3	10.4
25.75	179.3	9.4
26.25	174.3	9.2
26.75	178.4	8.1
27.25	176.9	8.2

Note. Columns show the Galactocentric radius, the circular velocity, and its error bar.

Khoperskov et al. 2020; Wang et al. 2023), which implies that the hypotheses used to obtain the Galaxy rotation curve, such as the time-independent Jeans equation and a smooth and monotonic density distribution, must be considered as approximations to the actual dynamics. Constructing a theoretical, self-consistent description of the galaxy that can relate these streaming motions in all velocity components to spatial structures is a challenging task. The gravitational influence of various galactic components, such as the long bar or bulge, spiral arms, or a tidal interaction with the Sagittarius dwarf galaxy, may explain some features of the observed velocity maps, particularly in the inner parts of the disk. However, in the outermost regions, the main observed
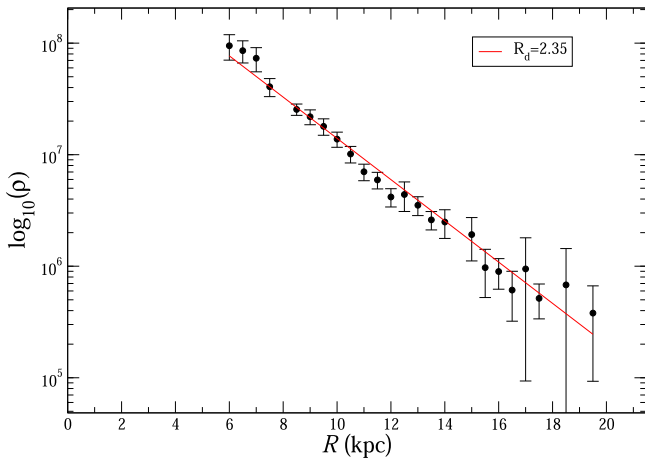
Figure 1. Dependence of the stellar density from the Gaia EDR3 data set on the Galactocentric distance in the Galactic equatorial plane for the azimuth $\phi \in [330°; 30°]$ (see Chrobáková et al. 2022 for details).

features can only be explained by out-of-equilibrium models, which are either due to external perturbers or to the fact that the disk has not had enough time to reach equilibrium since its formation (López-Corredoira et al. 2020).

Chrobáková et al. (2020) found that, as long as the amplitude of the radial velocity component is small compared to that of the azimuthal one, the Jeans equation provides a reasonable approximation to the system dynamics. Kinematic maps derived from the Gaia DR3 data set in the Galactic plane up to 30 kpc show that perturbations in the radial velocity are small enough so that using the time-independent Jeans equation to compare observations with theoretical models is justified (Wang et al. 2023).

A standard practice in mass modeling of external galaxies is to numerically solve the Poisson equation for the observed surface brightness distribution, which allows for nonmonotonic variations in the surface density profile and/or the presence of bumps and wiggles to be taken into account (Sellwood 1999; Palunas & Williams 2000; De Blok et al. 2008). The specific pattern of bumps and wiggles in its density profile should leave a distinctive imprint on the predicted rotation curve (Sancisi 2004). Both Eilers et al. (2019) and Wang et al. (2023) have assumed that the volume mass density of matter has an exponential decay. Here, instead of assuming the exponential function, the surface stellar density profile was computed from the star distribution in the Gaia EDR3 data set (Chrobáková et al. 2022) and the logarithmic gradient of this profile was numerically computed. This same method was used by McGaugh (2019) who determined at small radii, i.e., $R < 8$ kpc, the influence of spiral arms on the rotation curve. The observed stellar profile for $R > 8$ kpc, reported in Figure 1, does not have particular features and is well approximated by an exponential decay, which is why the analytical approximation works quite well, and the differences with the observed one are smaller than the reported error bars.

Finally, in order to estimate systematic uncertainties on the circular velocity curve arising from the data sample, following Wang et al. (2023), the galactic region was split into two disjoint smaller portions, one with galactic latitude $b > 0°$ and the other with $b < 0°$ or one with $Z > 0$ and one with $Z < 0$. The rotation curve was then computed in the two disjoint regions and the systematic uncertainties on the circular velocity were estimated from the difference between the resulting fit

parameters from the two disjoint data sets. We find that the rotation curves obtained are within the reported error bars, leading to the conclusion that systematic fluctuations, such as those due to local structures, should not give a large contribution. With these hypotheses in mind, the rotation curve data can be used to fit different mass models.

4. Mass Models

Given the profile of the rotation curve $v_c(R)$ presented in the last section and reported in Table 1, we can now determine the parameters of the theoretical models. Following Eilers et al. (2019) we assume that the stellar components consist of the bulge, the thin disk, and the thick disk. We take the same characteristic values of these components as in Eilers et al. (2019): The final results do not qualitatively depend on this choice, but they do quantitatively. Because Poisson's equation is linear, both the gravitational potential and the square of the rotation $v_c(R)$ are a linear sum of the various components, i.e.,

$$\Phi = \sum_i \Phi_i \Rightarrow v_c^2 = \sum_i v_{c,i}^2. \quad (2)$$

The rotation velocity $v_{c,i}$ is defined as the velocity that the ith mass component would induce on a test particle in the plane of the galaxy if it were placed in isolation without any external influences. These velocities in the plane are calculated from the observed stellar-mass density distributions plus the one due to the assumed DM distribution.

The first mass model considered in addition to the stellar components takes into account the velocity contribution of the DM halo with an NFW profile (Navarro et al. 1997). This model has only two free parameters describing the NFW profile, which are bound by a phenomenological relation (Macciò et al. 2008). The second mass model assumes the DM component to be distributed on the Galactic disk in agreement with the "Bosma effect." Two different scenarios are considered in this model. In the first case, DM is distributed on a thin disk with an exponentially decaying surface density profile, where the characteristic length of the profile R_d and the total disk mass M_d are considered free parameters. In the second case, the functional behavior of the DM surface density is assumed to be the same as that of the observed Galactic gas distribution, where the length scale R_d is that characterizing the gas surface density. and the unique free parameter of the model is the disk total mass M_d. Finally, the third mass model assumes only the stellar-mass components, but in the MOND framework. In this case, the stellar disk characteristic length scale R_d and mass M_d are considered free parameters.

4.1. Disk and Bulge Components

For the gravitational potentials of the thin and thick disk, Eilers et al. (2019) used Miyamoto–Nagai profiles (Miyamoto & Nagai 1975), while for the bulge they assume a spherical Plummer potential (Plummer 1911). In addition, they adapted the parameter values of the enclosed mass, the scale length, and the scale height from Pouliasis et al. (2017) (model I). We follow here this same approximation for the stellar components so that we find the thin disk has a characteristic length scale $R_{thin} \approx 4.5$ kpc and $M_{thin} \approx 3 \times 10^{10} M_\odot$, and the thick disk has $R_{thick} \approx 2.3$ kpc and $M_{thick} \approx 2.7 \times 10^{10} M_\odot$. Models of the bulge give a total bulge mass $M_{bulge} \approx 2 \times 10^{10} M_\odot$ with $R_{bulge} \approx 0.25$ kpc (Jurić et al. 2008; Bland-Hawthorn & Gerhard 2016). The characteristic
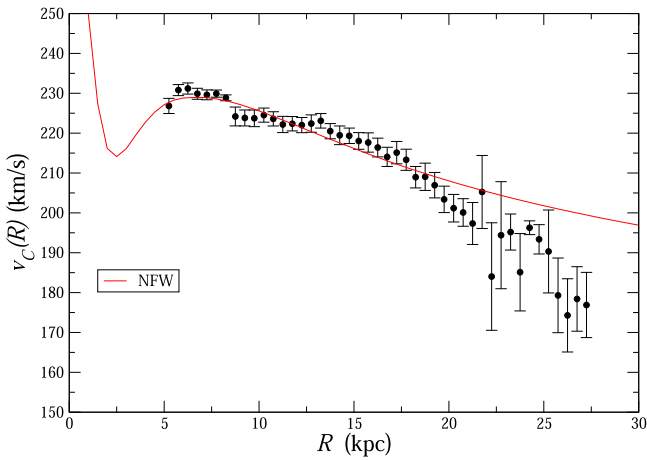
Figure 2. Best fit of the NFW mass model to the rotation curve given in Table 1 (DR3+ determination of the rotation curve).

length of the bulge, $R_{\mathrm{bulge}} \approx 0.25$ kpc, is small enough that the bulge contribution is relevant only at very small scales where the rotation curve is not well determined. In addition, note that the value of the mass of the bulge $M_{\mathrm{bulge}} \approx 2 \times 10^{10} M_{\odot}$ is about twice larger as that used by Eilers et al. (2019).

The total mass of the stellar components, with these approximations, is $M_{\mathrm{stellar}} \approx 8 \times 10^{10} M_{\odot}$.

4.2. The NFW Halo Model

The NFW mass model can be written as

$$v_c^2 = v_{\mathrm{thin}}^2 + v_{\mathrm{thick}}^2 + v_{\mathrm{bulge}}^2 + v_{\mathrm{NFW}}^2, \qquad (3)$$

where v_{NFW} corresponds to the equilibrium velocity in an NFW profile described by (Navarro et al. 1997)

$$\rho(r) = \frac{\rho_0}{\frac{r}{R_s}\left(1 + \frac{r}{R_s}\right)^2}, \qquad (4)$$

where R_s and ρ_0 are two free parameters. Results can be expressed in terms of the virial radius, where the mean density of the halo reaches a value 200 times that of the mean cosmic mass density, $R_{\mathrm{vir}} = cR_s$, and the halo virial mass is $M_{\mathrm{vir}} = M(R_{\mathrm{vir}})$, where c is the concentration parameter (Navarro et al. 1997).

The best-fit model is found by minimizing the reduced χ_ν^2, where $\nu = N_{\mathrm{data}} - 2$ as there are two free parameters in the model. Results are shown in Figure 2: Note that the increase of the rotation curve for small radii is due to the effect of the bulge. In Table 2 we report the values of the NFW best-fit parameters. When we use the determination of the rotation curve by Eilers et al. (2019), our best-fit parameters coincide, within the error bars, with theirs (note that, in this case, we used $M_{\mathrm{bulge}} \approx 1 \times 10^{10} M_{\odot}$ to make a fit directly comparable). The values of R_{vir} and M_{vir} are the smallest for the DR3 determination of the rotation curve that does not cover the range of radii for $R < 8$ kpc; for the case DR3+, they are intermediate between the DR3 and the E19 case. The variations of the fitted parameters that we find in the different sample have a simple explanation in terms of the finite range of radii accessible to observations that extend to only about 15% of $R_{\mathrm{vir}} \approx 200$ kpc and because the data for $R > 20$ kpc have little leverage on the fit (see discussion in de Blok et al. 2001).

Table 2
Results of the Best Fits of an NFW Model to the Three Determinations of the Rotation Curve (RC) We Considered (E19 is by Eilers et al. 2019, DR3 is by Wang et al. 2023, and DR3+ is Presented in Table 1—See Text)

RC	M_{vir}	R_{vir}	c	c_{NFW}	χ_ν^2
E19	80 ± 2	197 ± 2	13.0 ± 0.5	7.2 ± 1	2.1
DR3	48 ± 3	166 ± 3	19.6 ± 0.5	7.6 ± 1	2.4
DR3+	65 ± 3	183 ± 3	14.5 ± 0.5	7.3 ± 1	1.8

Note. We used $H_0 = 69$ km^{-1} s^{-1} Mpc^{-1} as the value of Hubble's constant. The mass M_{vir} is in units of $10^{10} M_{\odot}$ and the radius R_{vir} in kiloparsec.

Considering the stellar contributions, the total mass of the MW (i.e., halo and stellar components) for the best fit of the DR3+ rotation curve is thus $(73 \pm 3) \times 10^{10} M_{\odot}$ inside a virial radius of $R_{\mathrm{vir}} = 183 \pm 1.84$ kpc. In this model, the DM halo becomes the dominant dynamical contribution for $R > 15$ kpc, whereas the inner part is dominated by the stellar components.

Normally, NFW profiles are characterized by two model parameters (Navarro et al. 1997), and mass model fits usually consider both parameters free (see, e.g., De Blok et al. 2008; Eilers et al. 2019). However, it was then shown by Macciò et al. (2008) that the N-body calculations that resulted in the NFW profile model clearly show that the concentration parameter c is not an independent parameter but is in fact strongly correlated with V_{vir}; the rotational velocity at R_{vir} can be written as (Hessman & Ziebart 2011)

$$c_{\mathrm{NFW}} \approx 7.80 \left(\frac{V_{\mathrm{vir}}}{100 \ \mathrm{km \ s^{-1}}}\right)^{-0.294} \qquad (5)$$

(derived from Equation (10) of Macciò et al. 2008—see Dutton & Maccio 2014 for a slightly different phenomenological fit). Including this intrinsic correlation reduces the number of fit parameters by one. In Table 2, the values of the best-fit concentration parameter c and c_{NFW} computed from Equation (5) by inserting the value of the rotational velocity at R_{vir} are reported. It is noticed that in all cases, these are not consistent with the predictions of ΛCDM, which provides the well-defined mass–concentration relation, Equation (5). We thus find that the Galactic halo has a concentration parameter $c \in (13, 20)$, which is higher than theoretical expectations based on cosmological simulations (Macciò et al. 2008). High values of the concentration parameter have also been found by other studies: Bovy et al. (2012), Deason et al. (2012), Kafle et al. (2014), McMillan (2017), Monari et al. (2018), Lin & Li (2019), and Eilers et al. (2019), which are in tension with theoretical expectations based on cosmological simulations.

It should be noted that the potential systematic effect of adiabatic compression was not taken into account in the mass models. Adiabatic compression is an inevitable mechanism that occurs when a luminous galaxy is formed within a DM halo (Gnedin et al. 2004; Sellwood & McGaugh 2005). This process may help reconcile the parameters found with Equation (5) as it has the effect of raising the effective concentration of the resulting halo above that of the primordial initial condition to which the mass–concentration relation applies (McGaugh 2016). This means that the higher-than-expected concentration of the MW halo could be a manifestation of the contraction of the DM

halo induced by the presence of a galaxy at its center (Cautun et al. 2020). However, it should be noted that there are contradictory statements about the adiabatic compression of our Galaxy's dark halo in the literature; for instance, Binney & Piffl (2015) find evidence that rules it out.

4.3. The Dark Matter Disk Model

As discussed above the "Bosma effect" assumes a correlation between the distribution of DM and that of the gas so that the rotation curve can be written as

$$v_c^2 = v_{\text{thin}}^2 + v_{\text{thick}}^2 + v_{\text{bulge}}^2 + \Upsilon_{\text{gas}} v_{\text{gas}}^2, \qquad (6)$$

where v_{gas} is the circular velocity of the gas, and Υ_{gas}, the ratio between the DM and gas mass, is an appropriate rescaling factor that must be determined in order to fit the observed rotation curve.

For the case of external galaxies, it is observed only in the distribution of neutral H I, and not that of total gas; for this reason, Hessman & Ziebart (2011) parameterized the model as

$$v_c^2 = \Upsilon^* (v_{\text{thin}}^2 + v_{\text{thick}}^2 + v_{\text{bulge}}^2) + \Upsilon_{\text{HI}} v_{\text{H I}}^2, \qquad (7)$$

where Υ^* is an additional free parameter introduced because the H I surface density does not reflect the total gas surface density in the inner galactic region and the stellar disk was used as a proxy of a dark mass component. In the case of the MW, both the radial atomic (HI) gas (Kalberla & Kerp 2009) and the molecular gas (H_2) surface density profiles are available (Bigiel & Blitz 2012).

We consider two different functional behaviors for the gas surface density: (i) An exponential surface density on a thin disk (TD) and (ii) the sum of H I and H_2 confined on a TD. In the first case, the free parameters are the exponential length scale R_d and the total mass M_d, while in the second case, only the mass is considered. The comparison between these two different behaviors of the gas surface density allows us to understand the effect of the functional dependence of the gas component on the final mass estimate.

For the first case, we used the well-known result that the circular velocity generated by an exponentially decaying surface mass density

$$\Sigma(R) = \Sigma_0 \exp\left(-\frac{R}{R_d}\right), \qquad (8)$$

(with total mass total equal to $M_d = 2\pi \Sigma_0 R_d^2$) constrained on a TD is (see, e.g., Binney & Tremaine 2008)

$$v_c^2(R) = 4\pi G \Sigma_0 R_d y^2 [I_0(y) K_0(y) - I_1(y) K_1(y)], \qquad (9)$$

where $y = R/2R_d$ and I_n and K_n are the modified Bessel functions. Results for this model are shown in Figure 3 and in Table 3: The smallest value of χ_ν^2 is found for the DR3+ rotation curve. This is smaller than that for the NFW model: This can be seen by comparing the large-radius behaviors in Figures 2–3. As in the previous case, the increase of the rotation curve for small radii is due to the effect of the bulge. The estimated mass of the DMD, i.e., $M_{\text{DMD}} \approx 15 \times 10^{10} M_\odot$ (with a characteristic scale length $R_d \approx 15$ kpc) is about a factor of 2 larger than the mass of all the stellar components (i.e., $M_{\text{stellar}} \approx 8 \times 10^{10} M_\odot$), and it is about a factor of 7 smaller than the virial mass of the NFW halo mass model. Note the Galaxy's
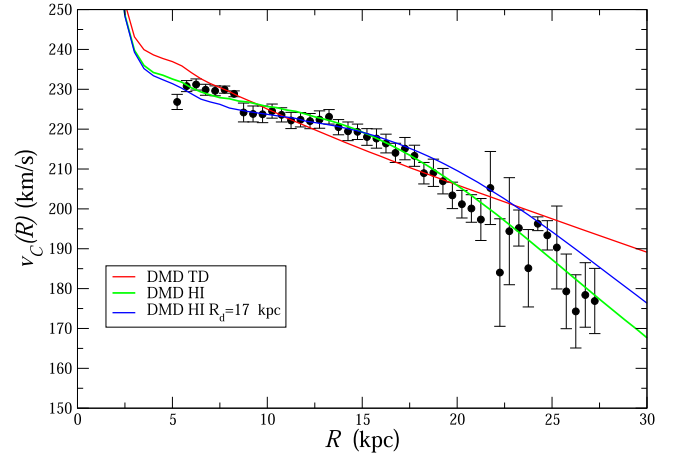

Figure 3. Best fit of the DMD mass model (i.e., Equation (7)) to the rotation curve given in Table 1 (DR3+ rotation curve). We show results for an exponentially decaying surface mass on a thin disk (Equations (8)–(9)), the case in which the surface density is given by Equation (10) with R_d and M_d as free parameters and the same but with $R_d = 17$ kpc (corresponding to the value measured for the distribution of Galactic H I) and only the DM disk's mass M_d as a free parameter.

Table 3
Results of the Best Fits of a DMD model (i.e., Equation (7)) for an Exponentially Decaying Surface Mass Density on a Thin Disk (Equations (8)–(9)) to the Three Determinations of the Rotation Curve We Considered

RC	R_d	M_d	χ_ν^2
E19	10.6 ± 0.2	16.3 ± 1	2.0
DR3	8.8 ± 0.2	12.4 ± 1	1.4
DR3+	10.2 ± 0.2	15.2 ± 1	1.3

Note. Units are R_d in kiloparsec and M_d in $10^{10} M_\odot$.

mass in the NFW model must include the contribution of the halo up to the virial radius, i.e., $R_{\text{vir}} \approx 180$ kpc; instead, by assuming that DM is confined on a disk the mass of the galaxy, M_d is the one corresponding to a characteristic disk's radius $R_d \approx 15$ kpc.

We now assume that the observed atomic H I and molecular H_2 distribution traces that of DM. We found that a useful approximation to the observed surface density of H I, reported in Kalberla & Kerp (2009) and Bigiel & Blitz (2012), is given by (see the upper panel of Figure 4)

$$\Sigma_{\text{HI}}(R) = \frac{\Sigma_0}{1 + \left(\frac{R}{R_d}\right)^\alpha}, \qquad (10)$$

with $\Sigma_0 \approx 6 M_\odot$ pc^{-2}, $R_d = 17$ kpc, and $\alpha = 10$ (this corresponds to a total H I mass of $M_{\text{HI}} \approx 0.5 \times 10^{10} M_\odot$). For the observed surface density of H I+H_2 (Bigiel & Blitz 2012), we find that there is a small difference at small radii, i.e., $R < 4$ kpc, that we parameterize, for $R > 2$ kpc, as

$$\Sigma_{\text{HI}+H_2}(R) = \frac{\Sigma_0}{\left(1 + \left(\frac{R}{R_d}\right)^\alpha\right)\left(\frac{R}{R_d}\right)^{0.25}}. \qquad (11)$$
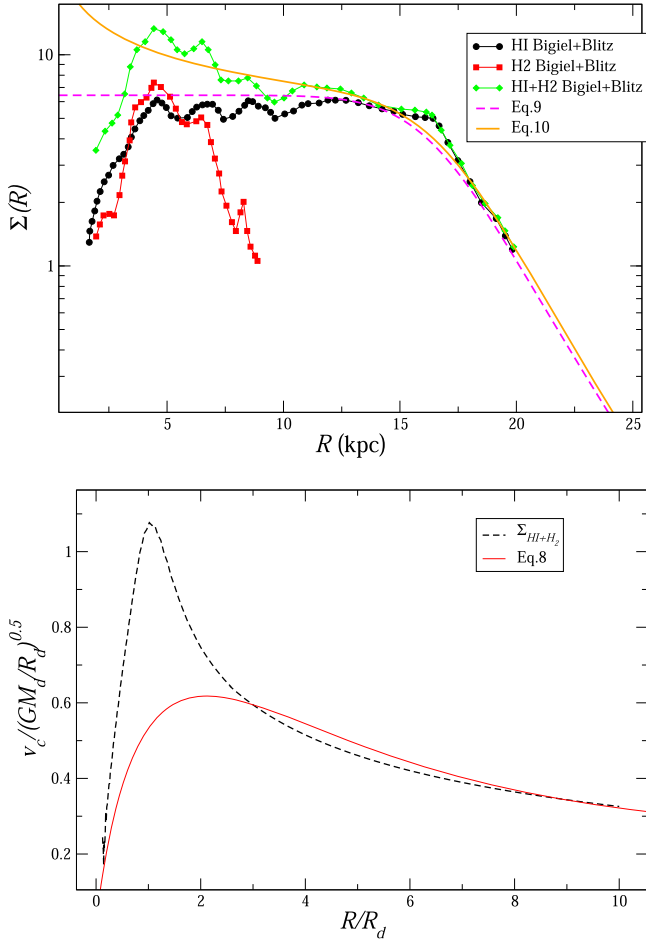
Figure 4. Upper panel: surface density profile in Equation ([10](#)) (solid line) (in $M_\odot$ pc^{-2}) and data from Kalberla & Kerp ([2009](#)) and Bigiel & Blitz ([2012](#)). Bottom panel: circular velocity of a distribution of matter confined on a thin disk with a surface density profile in Equation ([10](#)) together with the behavior of Equation ([9](#)).

Note that these approximations are useful only as they give an analytical reference but are not used in what follows to compute the circular velocity.

Given the surface density profile in Equation ([11](#)), it is possible to compute the corresponding gravitational potential and, from it, the circular velocity v_c. Unlike the case of a spherical mass distribution, in the case of a disk, the result that the mass distribution outside a particular radius does not affect the effective force inside that radius is not universally valid. For this reason, we numerically computed the circular velocity of a distribution of matter confined on a disk, with a height equal to $1/20$ of its radius and with the observed gas surface density profile. The behavior of the circular velocity is shown in Figure [4](#) (bottom panel) together with the behavior for an exponentially decaying surface mass density confined on a TD (i.e., Equation ([9](#))).

The results of this model are shown in Figure [3](#) and in Table [4](#). Note that the value of the mass is smaller than the previous case by $\approx 40\%$, that is, the DM component is about the same as the visible mass component, i.e., $M_{DMD} \approx 9 \times 10^{10} M_\odot$, and it is about a factor of 6 smaller than the viral mass of the NFW halo. Finally, we note that the DM mass is about 20 times heavier than that of H I, as $M_{H\,I} \approx 0.5 \times 10^{10} M_\odot$: this value is comparable with what was found in

Table 4
In This Case the Surface Density of Dark Matter is Assumed to be Traced by That of H I, i.e., It is Proportional to Equation ([10](#))

RC	R_d	M_d	χ_ν^2
E19	11.6 ± 0.2	15.1 ± 0.5	2.6
DR3	15.6 ± 0.5	8.5 ± 0.5	1.2
DR3	17.0	10.0 ± 0.5	1.7
DR3+	15.5 ± 0.5	8.5 ± 1	1.2
DR3+	17.0	9.7 ± 1	2.3

Note. Two different cases are considered with the DR3 and DR3+ determinations of the rotation curve: In the first, both R_d (in kiloparsec) and M_d (in $10^{10} M_\odot$) are free parameters and in the second, $R_d = 17$ kpc, as measured from the distribution of Galactic H I, and M_d is a free parameter.

external galaxies by Hessman & Ziebart ([2011](#)) and Swaters et al. ([2012](#)).

4.4. The MOND Model

Finally, we have fitted the rotation curve in the MOND framework (Milgrom [1983](#)). It is worth noting that a similar study was presented in Chrobáková et al. ([2020](#)) using Gaia DR2 data, which reached distances up to $R \approx 20$ kpc and heights only up to $|Z| < 2$ kpc, where the decreasing trend in the MW rotating curve was less noticeable. Additionally, as discussed by Wang et al. ([2023](#)), the binning of data in Chrobáková et al. ([2020](#)) was finer, leading to larger noise fluctuations and making the signal less reliable. Thus, the rotation curves of Chrobáková et al. ([2020](#)) are less robust than our current analysis, and the trends we see now were not noticed then.

We follow the approach of Chrobáková et al. ([2020](#)) and calculate the MONDian acceleration as

$$a_M = \sqrt{\frac{1}{2}a_N^2 + \sqrt{\frac{1}{4}a_N^4 + a_N^2 a_0^2}} \,, \qquad (12)$$

where the constant $a_0 = 1.2 \cdot 10^{-10}$ m s^{-2} (Scarpa [2006](#)) and the Newtonian acceleration a_N can be calculated as (McGaugh et al. [2016](#))

$$a_N = \left| \frac{v_c^2(R)}{R} \right| \,, \qquad (13)$$

where v_c is the full, Newton-predicted rotation curve. Since this model does not include a halo, we consider the M_d and R_d of the stellar disk as free parameters, and we do not fit the bulge as this involves radii that are smaller than those sampled by the measured rotation curves. In Figure [5](#) we plot the best fit of the MOND model of the DR3+ determination of the rotation curve. The fit for the sample from the DR3 determination of the rotation curve is worse than the other two samples, as the DR3 sample lacks data for radii $R < 10$, which are fitted better than the data at the largest radii. In addition, the MOND model best fit has the minimum value of the χ_ν^2 only if we also use the disk's mass and radius as free parameters rather than using the fixed values of the stellar component as discussed above (see Section [4.1](#)). We get that $M_d = (7.8 \pm 0.5) \times 10^{10} M_\odot$ and
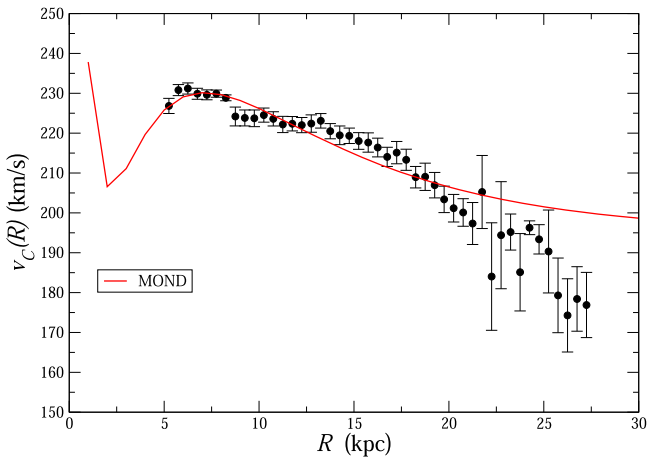
Figure 5. Best fit of the MOND model to the rotation curve given in Table 1. The red curve represents the MOND model with parameters fixed with values $R_d = 3.1$ kpc, $M_{\text{thin}} = 7.79 \times 10^{10} M_{\odot}$.

$R_d = (3.1 \pm 0.1)$ kpc: Both values are larger than those used in Section 4.1.

However, note that Equation (12) is an approximation of the exact MOND relation, producing a small difference compared to the exact approach (López-Corredoira & Betancort-Rijo 2021). To estimate how much our solution deviates from the exact calculation, we use the results of López-Corredoira & Betancort-Rijo (2021), who compare the difference between the approximation and the exact solution for an exponential disk (Figures 2 and 3 of their paper). Based on their result, we estimate that the rotation curve for our model deviates by 5%–10%. Therefore, we make Monte Carlo simulations, taking into account this deviation and calculate new parameters of the fit, which we use to calculate the systematic errors of the free parameters (reported in Table 5).

Another aspect to consider is that the Jeans Equation used to derive the rotation curve in Wang et al. (2023) assumes a Newtonian potential instead of MOND. Strictly, one should use the Poisson equation

$$\nabla(\mu(x)\nabla\phi) = 4\pi G\rho,$$

where

$$x = \frac{|\vec{g}(\vec{r})|}{a_0}$$

and $\vec{g}$ is the acceleration, instead of the Newtonian one, $\nabla^2\phi = 4\pi G\rho$. However, the consequence of this MOND factor μ would be equivalent to adding a phantom mass to the real mass density distribution ρ (López-Corredoira & Betancort-Rijo 2021). The problem of the modification of the Poisson equation implicitly included in Jeans equation is simply solved by changing the real density by an equivalent density including a phantom term (see Equation (12) of López-Corredoira & Betancort-Rijo 2021). In our case, we have assumed an exponential function for ρ, and this is also an appropriate assumption for the equivalent density in MOND including the phantom term. Moreover, the outcome of the rotation speed is very little affected by the scale length of the exponential distribution (Chrobáková et al. 2020). Therefore, we do not think the rotation speed might be significantly affected beyond

Table 5
Results of the Best Fit for the MOND Model

Sample	R_d	M_d	χ_c^2
E19	3.2 ± 0.1 (stat.) $\pm$ 0.18 (syst.)	7.97 ± 0.1 (stat.) $\pm$ 0.9 (syst.)	1.46
DR3	2.8 ± 0.29 (stat.) $\pm$ 0.2 (syst.)	7.24 ± 1.5 (stat.) $\pm$ 1.0 (syst.)	5.79
DR3+	3.1 ± 0.1 (stat.) $\pm$ 0.14 (syst.)	7.79 ± 0.5 (stat.) $\pm$ 0.7 (syst.)	2.32

Note. R_d is in kiloparsec, M_d is in units of $10^{10} M_{\odot}$. We report both the statistical (stat.) and systematic (syst.) errors.

the error bars due to the MOND modification of the Jeans equation.

In summary, the MW rotation curve is extremely well fitted by MOND up to $R = 19$ kpc. The region where MOND poorly fits the data is for $R > 20$ kpc, i.e., where the rotation curve is found to decline both by Eilers et al. (2019) and Wang et al. (2023). This result thus confirms earlier studies by McGaugh (2016, 2019) at smaller radii, i.e., $R < 10$ kpc. It is worth mentioning that McGaugh (2019) considered a model for the MW obtained by fitting the observed terminal velocities with the radial-acceleration relation. Such a model predicts a gradually declining rotation curve outside the solar circle with a slope of -1.7 km s^{-1} kpc^{-1}, as subsequently observed by Eilers et al. (2019).

5. Conclusions

The MW has several baryonic components, including a central nucleus, a bulge, and a disk. While many of their properties remain topics of debate, their masses are reasonably well determined (Bland-Hawthorn & Gerhard 2016). From kinematical and dynamical studies, we know that the mass of the MW must be larger than the sum of the baryonic components; indeed, to maintain the system in stable equilibrium with the observed amplitude of the circular velocity, a large fraction of the MW mass must be invisible, i.e., we cannot measure it directly, but we can infer its presence by its gravitational influence.

Despite decades of intense efforts, the estimates of the mass of the MW still show significant scatter. These estimates are very sensitive to assumptions made in the modeling and, in particular, to the shape of the halo in which the Galaxy is embedded. Most mass estimators are limited to the region explored by the available tracer population, whose spatial distribution and kinematics are used to estimate the enclosed mass. Estimates of the MW's mass have been obtained based on the kinematics of halo stars, the kinematics of satellite galaxies and globular clusters, the evaluation of the local escape velocity, and the modeling of satellite galaxy tidal streams. Estimates typically range from as low as $0.5 \times 10^{12} M_{\odot}$ to as high as $4 \times 10^{12} M_{\odot}$ (Bland-Hawthorn & Gerhard 2016). These estimates assume that dark matter (DM) is in a quasi-spherical virialized halo around the Galaxy (Navarro et al. 1997; Sanders 2010).

In this paper, we have presented a new estimation of the MW's virial mass in the framework of the NFW halo model. This estimation is based on combining two recent

determinations of the Galaxy's rotation curve by Eilers et al. (2019), in the range of 5–25 kpc, and by Wang et al. (2023), in the range of 8–28 kpc, so as to obtain the rotation curve in the range of 5–28 kpc. In both cases, the MW's rotation curve was measured in samples that are based, partially or completely, on data provided by the Gaia mission (Gaia Collaboration et al. 2016). These data have the unique characteristic of collecting the whole 6D spatial and velocity information of the sources with unprecedented precision and accuracy for the determination of their distances. Results for $v_c(R)$ by Eilers et al. (2019) and Wang et al. (2023) reasonably agree with each other and with another similar determination based on Gaia data but on a smaller distance range by Mróz et al. (2019). In short, the MW's rotation curve in these samples shows a gentle decline, passing from ≈ 230 km s^{-1} at 5 kpc to ≈ 175 km s^{-1} at 28 kpc. The data with $R > 20$ kpc are clearly important for the results of the fits and one may wonder whether we are pushing the data to its limits. We think that this is not the case for two reasons. First, the Lucy method, which is the basis of the rotation curve determined by Wang et al. (2023), has proven to be a solid technique that has given convergent results when passing from Gaia DR2 to Gaia DR3. The method works as long as errors in the parallax are Gaussian, and the fact that by lowering the errors, the results are convergent means that this is not only a reasonable approximation but it is verified in the data. Second, Eilers et al. (2019) have already shown that there is a significant difference in the range of 15–20 kpc with a flat rotation curve. Forthcoming data releases of the Gaia mission will provide more evidence that can possibly corroborate these results.

We find $M_{\rm vir} = (6.5 \pm 3) \times 10^{11} M_\odot$ within a virial radius $R_{\rm vir} = (180 \pm 3)$ kpc, which is $\approx 20\%$ smaller than the estimation by Eilers et al. (2019). This gives a significantly lower mass estimation than what several previous studies suggest (Bovy et al. 2012; Eadie & Harris 2016; Eadie et al. 2018). This is due to the fact that the rotation curve measured by Eilers et al. (2019) and Wang et al. (2023) showed a declining behavior up to 28 kpc, while most other determinations found $v_c(r) \approx$ const. at the same radii (see, e.g., Bhattacharjee et al. 2014; Sofue 2020 and references therein).

We have then considered an additional phenomenological constraint derived from N-body calculations (Macciò et al. 2008), which reduces the number of free parameters of the NFW profile from two to one. We find that in this case, the NFW fit parameters fall outside the predicted range of mass and concentration, so with this additional constraint (see Equation (5)), there is tension with expectations from simulations.

We then considered an alternative model for the distribution of DM in the Galaxy, called the DMD model. This model is inspired by the "Bosma Effect" (Bosma 1978, 1981) and assumes that the DM component is confined to a disk and is traced by the gas distribution. We find that the amount of DM in this model is a factor of 9 smaller than in the NFW case, being about the same as the visible mass component. We also found that the DMD models are statistically as good as the NFW ones. As DM is confined on a disk and not distributed in a spherical halo, it is not surprising that we find that its amount is a factor of 9 smaller than in the NFW case, being about the same as the visible mass component, i.e., $M_{\rm stellar} \approx 8 \times 10^{10} M_\odot \approx M_{\rm DMD}$ so that the total mass of the Galaxy, in this case, is $1.6 \times 10^{11} M_\odot$. In this case, the characteristic scale length of the disk is $R_d = 17$ kpc and the

DM mass is about 20 times heavier than that of H I, as $M_{\rm H\ I} \approx 0.5 \times 10^{10} M_\odot$: This value is in line with that found in external galaxies by Hessman & Ziebart (2011) and Swaters et al. (2012). The large-radius behavior of the rotation curve in this model is determined by that of the rescaled gas component. For this reason, it is worth noting that Bigiel & Blitz (2012) found that the azimuthally averaged radial distribution of the neutral gas surface density in a sample of nearby spiral galaxies that includes the MW exhibits a well-constrained universal exponential distribution beyond $0.2 \times r_{25}$: In the framework of the DMD model, this universal gas profile corresponds to the same large-radius (in units of r_{25}) rotation curve shape.

We find that the DMD models are statistically as good as the NFW ones. It should be emphasized that the DMD fits would not be as successful if the rotation curve did not show the decreasing behavior observed in samples based on the Gaia data set.

Finally, we considered a model based on the MOND framework (Milgrom 1983; Scarpa 2006; McGaugh et al. 2016), which does not assume the presence of a heavy DM halo or a DM disk but instead hypothesizes a slower decay of the gravitational force to equilibrate the rotation velocity with the observed stellar-mass components. We found that the data from the rotation curve of the MW is well described by the MOND mass model up to a distance of 19 kpc as previously found by, e.g., McGaugh et al. (2016). As for the case of the NFW model, the data for $R > 20$ kpc agree less well with the model because of the decreasing behavior of the rotation curve.

Overall, we can conclude that, from the point of view of compatibility with the observations of the rotation curve, the DMD hypothesis represents a plausible galactic model. However, this model requires further studies, and it is important to investigate the nature of the matter that can be confined in the disk and whether any possible candidate is compatible with the present state of the art. Additionally, refined modeling of this possible DM component and its compatibility with present observational constraints must be further investigated. In this respect, it is worth recalling that Pfenniger et al. (1994) suggested that such a dark component, or a fraction of it, might be in molecular form and distributed in cold clouds that still elude direct detection. A refined modeling of this possible DM component and its compatibility with present observational constraints is certainly worth investigating.

The near proportionality between H I and DM in outer galactic disks suggests that DM can be distributed on a disk rather than in a spherical halo. However, adding baryons to the disk of galaxies poses the problem of disk stability. It is well known that self-gravitating disks close to stationary equilibrium and dominated by rotational motions are remarkably responsive to small disturbances (see, e.g., Sellwood & Carlberg 1984, 2014, 2019; Binney & Tremaine 2008; Dobbs et al. 2018 and references therein). Revaz et al. (2009) have shown that global stability is ensured if the interstellar medium is multiphased, composed of two partially coupled phases: a visible warm gas phase and a weakly collisionless cold dark phase corresponding to a fraction of the unseen baryons. This new model still possesses a DM halo as in CDM ones. A different theoretical scenario occurs if the disk originated from a top-down gravitational collapse of an isolated overdensity. Benhaiem et al. (2019) and Sylos Labini et al. (2020) have shown that this scenario may improve the resistance to the

effect of internal or external perturbations. A more detailed investigation of the stability of these systems and of a cosmological model for their formation will be presented in a forthcoming work.

ORCID iDs

Francesco Sylos Labini ⬥ https://orcid.org/0000-0003-2236-4537
Žofia Chrobáková ⬥ https://orcid.org/0000-0002-9895-6638
Martín López-Corredoira ⬥ https://orcid.org/0000-0001-6128-6274

References

Antoja, T., Helmi, A., Romero-Gomez, M., et al. 2018, Natur, 561, 360
Benhaiem, D., Sylos Labini, F., & Joyce, M. 2019, PhRvE, 99, 022125
Bhattacharjee, P., Chaudhury, S., & Kundu, S. 2014, ApJ, 785, 63
Bigiel, F., & Blitz, L. 2012, ApJ, 756, 183
Binney, J., & Piffl, T. 2015, MNRAS, 454, 3653
Binney, J., & Tremaine, S. 2008, Galactic Dynamics (Princeton, NJ: Princeton Univ. Press)
Bland-Hawthorn, J., & Gerhard, O. 2016, ARA&A, 54, 529
Bosma, A. 1978, PhD thesis, Univ. Groningen
Bosma, A. 1981, AJ, 86, 1791
Bovy, J., Allende Prieto, C., Beers, T. C., et al. 2012, ApJ, 759, 131
Cautun, M., Benitez-Llambay, A., Deason, A. J., et al. 2020, MNRAS, 494, 4291
Chrobáková, Ž., López-Corredoira, M., Sylos Labini, F., Wang, H.-F., & Nagy, R. 2020, A&A, 642, A95
Chrobáková, Ž., Nagy, R., & López-Corredoira, M. 2022, A&A, 664, A58
de Blok, W. J. G., McGaugh, S. S., Bosma, A., & Rubin, V. C. 2001, ApJL, 552, L23
De Blok, W. J. G., Walter, F., Brinks, E., et al. 2008, AJ, 136, 2648
Deason, A. J., Belokurov, V., Evans, N. W., & An, J. 2012, MNRAS, 424, L44
Dobbs, C. L., Pettitt, A. R., Corbelli, E., & Pringle, J. E. 2018, MNRAS, 478, 3793
Dutton, A. A., & Macciò, A. V. 2014, MNRAS, 441, 3359
Eadie, G., Keller, B., & Harris, W. E. 2018, ApJ, 865, 72
Eadie, G. M., & Harris, W. E. 2016, ApJ, 829, 108

Eilers, A.-C., Hogg, D. W., Rix, H.-W., & Ness, M. K. 2019, ApJ, 871, 120
Gaia Collaboration, Katz, D., Antoja, T., et al. 2018, A&A, 616, A11
Gaia Collaboration, Prusti, T., de Bruijne, J. H. J., et al. 2016, A&A, 595, A1
Gaia Collaboration, Vallenari, A., & Brown, A. G. A. 2022, arXiv:2208.00211
Gnedin, O. Y., Kravtsov, A. V., Klypin, A. A., & Nagai, D. 2004, ApJ, 616, 16
GRAVITY Collaboration, Abuter, R., Amorim, A., et al. 2018, A&A, 615, L15
Hessman, F. V., & Ziebart, M. 2011, A&A, 532, A121
Hoekstra, H., van Albada, T. S., & Sancisi, R. 2001, MNRAS, 323, 453
Jurić, M., Ivezić, Ž., Brooks, A., et al. 2008, ApJ, 673, 864
Kafle, P. R., Sharma, S., Lewis, G. F., & Bland-Hawthorn, J. 2014, ApJ, 794, 59
Kalberla, P. M. W., & Kerp, J. 2009, ARA&A, 47, 27
Khoperskov, S., Gerhard, O., Di Matteo, P., et al. 2020, A&A, 634, L8
Lin, H.-N., & Li, X. 2019, MNRAS, 487, 5679
López-Corredoira, M., & Betancort-Rijo, J. E. 2021, ApJ, 909, 137
López-Corredoira, M., Garzon, F., Wang, H.-F., et al. 2020, A&A, 634, A66
López-Corredoira, M., & Sylos Labini, F. 2019, A&A, 621, A48
Lucy, L. B. 1977, AJ, 82, 1013
Macciò, A. V., Dutton, A. A., & van den Bosch, F. C. 2008, MNRAS, 391, 1940
McGaugh, S. S. 2016, ApJ, 816, 42
McGaugh, S. S. 2019, ApJ, 885, 87
McGaugh, S. S., Lelli, F., & Schombert, J. M. 2016, PhRvL, 117, 201101
McMillan, P. J. 2017, MNRAS, 465, 76
Milgrom, M. 1983, ApJ, 270, 365
Miyamoto, M., & Nagai, R. 1975, PASJ, 27, 533
Monari, G., Famaey, B., Carrillo, I., et al. 2018, A&A, 616, L9
Mróz, P., Udalski, A., Skowron, D. M., et al. 2019, ApJL, 870, L10
Navarro, J. F., Frenk, C. S., & White, S. D. M. 1997, ApJ, 490, 493
Palunas, P., & Williams, T. B. 2000, AJ, 120, 2884
Pfenniger, D., Combes, F., & Martinet, L. 1994, A&A, 285, 79
Plummer, H. C. 1911, MNRAS, 71, 460
Pouliasis, E., Di Matteo, P., & Haywood, M. 2017, A&A, 598, A66
Revaz, Y., Pfenniger, D., Combes, F., & Bournaud, F. 2009, A&A, 501, 171
Sancisi, R. 1999, Ap&S, 269, 59
Sancisi, R. 2004, in IAU Symp. 220, Dark Matter in Galaxies, ed. S. D. Ryder et al. (San Francisco, CA: ASP), 233
Sanders, R. H. 2010, The Dark Matter Problem: A Historical Perspective (Cambridge: Cambridge Univ. Press)
Scarpa, R. 2006, in AIP Conf. Ser. 822, First Crisis in Cosmology Conference, ed. E. J. Lerner & J. B. Almeida (Melville, NY: AIP), 253
Sellwood, J. A. 1999, in ASP Conf. Ser. 182, Galaxy Dynamics—A Rutgers Symposium, ed. D. R. Merritt, M. Valluri, & J. A. Sellwood (San Francisco, CA: ASP), 351
Sellwood, J. A., & Carlberg, R. G. 1984, ApJ, 282, 61
Sellwood, J. A., & Carlberg, R. G. 2014, ApJ, 785, 137
Sellwood, J. A., & Carlberg, R. G. 2019, MNRAS, 489, 116
Sellwood, J. A., & McGaugh, S. S. 2005, ApJ, 634, 70
Sofue, Y. 2020, Galax, 8, 37
Swaters, R. A., Sancisi, R., van der Hulst, J. M., & van Albada, T. S. 2012, MNRAS, 425, 2299
Sylos Labini, F., Pinto, L. D., & Capuzzo-Dolcetta, R. 2020, PhRvE, 102, 042108
Wang, H.-F., Chrobáková, Ž., López-Corredoira, M., & Sylos Labini, F. 2023, ApJ, 942, 12
Watkins, L. L., van der Marel, R. P., Sohn, S. T., & Wyn Evans, N. 2019, ApJ, 873, 118